A small-Scale Low-Cost Technology Demonstrator of a reusable Launch Vehicle

S. Chiesa*
Politecnico di Torino, 10129 Torino, Italy

M. Grassi†
Università di Napoli "Federico II", 80125 Napoli, Italy

G. Russo‡
Italian Aerospace Research Center, 81043 Capua, (CE), Italy

and

P. Teofilatto§
Scuola di Ingegneria Aerospaziale, Università di Roma La Sapienza, 00184 Roma, Italy

Recent years have seen an increasing interest of the scientific community toward the study and development of unmanned automatic vehicles, also in the Reusable Launch Vehicle (RLV) frame. Indeed, a number of unmanned vehicle projects have been devoted to demonstrate some key aspects of the technological challenges related to an autonomous RLV. The major efforts have been undertaken by NASA, with the past X-33 and X-34 programs. However, because of the high funding required by the development of a cost-effective completely reusable vehicle, current efforts are focused on developing demonstrators of some critical technologies of such a vehicle. Recent examples are the successful NASA's X-37/X-40 and DLR's Phoenix5, testing autonomous landing of an RLV-shaped vehicle, and the NASA X-43A6, testing air-breathing propulsion. In this framework, the Unmanned Space Vehicle (USV) Program7 is being performed by the Italian Aerospace Research Centre (CIRA). The USV Program main focus is on the development and in-flight testing of critical technologies of autonomous, fully re-usable, winged-body launch vehicles. To this end, three vehicles, named Flight Test Beds (FTB), will perform a number of missions aimed at gaining further insight into transonic and hypersonic flight, sub-orbital and orbital re-entry, guidance navigation and control, innovative thermal protection systems. In this context, a phase-A study of a low-cost reduced-scale technology demonstrator of a RLV has been carried out by research teams at Politecnico of Turin and at the universities of Naples and Rome under CIRA funding. The main goal of the study was to assess the feasibility of a reduced scale (1:5) technology demonstrator aiming at validating some critical technological and operational aspects of RLVs and of the USV program, by taking the Suborbital Re-entry Test (SRT) mission as case study. The SRT mission main objective is flying at thermal fluxes higher than 650 kW/m2 at the stagnation point for a time interval at least of 15 s ("hot time"), in order to test innovative Thermal Protection System (TPS) technologies. The vehicle, conceived as a result of the phase-A studies, is a two-stage system. The first stage consists of an expendable off-the-shelf solid propellant motor while the second stage is a non-propelled glider, whose aerodynamic shape is a scaled version of the full-scale USV vehicle. As a result of the phase-A studies, two candidate configurations have been identified for the vehicle, one (A) designed to attain high performance, in terms of

* Full Professor, Department of Aeronautics and Space Engineering, C.so Einaudi 40, 10129 Torino.
† Associate Professor, Department of Space Science and Engineering, 80125 Napoli.
‡ USV Program Manager, PMAS, CIRA, 81043 Capua (CE).
§ Full Professor, Department of Aerospace and Astronautics Engineering, 00184 Roma.

similarity with SRT, the other (B), taken as baseline configuration, to reduce system complexity and, mainly, cost.

I. An overview of the design process

The flow chart of the design process is illustrated in Fig. 1. The result of the feasibility study[1] has been the complete definition of two configurations of the demonstrator: Mini-FTB (Fig. 2) and Mini-FTB/A (Fig. 3). The main difference between the two versions is the propulsion system adopted: in fact, while Mini-FTB uses the rocket engine ATK STAR17, the Mini-FTB/A employs the ATK STAR17A, characterized by higher performances. Another difference between the two versions is the possibility for Mini-FTB of choosing between two types of cold gas for the RCS system, Nitrogen and Freon-14.

II. Requirements

A. Mission requirements

Mini-SRT mission requirements are listed as follows:

- sub-orbital flight: Mini-FTB has to perform a sub-orbital flight characterized by autonomous flight capability;
- data acquisition: Mini-FTB has to be able to perform data acquisition, processing and transmission, in order to support onboard operations, ground tracking of the flight and post flight analyses;
- sub-orbital ceiling height: the ceiling height requirement of 120 km or more must be met;
- thermal conditions during atmospheric flight: the maximum heat flux density requirement of 350 kW/m^2 or more must be met and sustained for at least 15 seconds;
- transonic flight: the requirement of 1÷1.1 Mach at 10÷15 km has to be met during re-entry;
- launch base: Trapani-Milo has to be considered as launch site of reference;
- altitude at vehicle's release: the nominal altitude allowed for vehicle's release from the carrier has to be higher than 20 km;
- safe separation between the vehicle and its carrier;
- radio link: radio uplink and downlink between the Mini-FTB and the ground station has to be available during the overall mission;
- landing phase: the vehicle's third stage, i.e. the Mini-FTB without its rocket engine, has to be recovered after its splash down;
- parachute system opening: the parachute has to be deployed at a speed lower than 0.6 Mach and at an altitude higher than 10000 m to allow for a safe deceleration phase;
- parachute system opening point dispersion: considering the splash down target, the parachute opening point of the third stage has to lay in the following ranges: ± 20 km of long range and ± 10 km of cross range. The occurrence of a larger ground dispersion area entails that the mission has been degraded;
- Mini-FTB reusability: the Mini-FTB has to be designed and manufactured to be recovered but not to be completely reusable;
- dynamic pressure: the maximum dynamic pressure requirement of 130 kPa has to be met during re-entry.

B. System requirements

Mini-FTB system requirements are listed as follows:

- launch configuration: Mini-SRT mission has to be performed by the following three stages: the carrier, constituted by a stratospheric balloon, as first stage, the Mini-FTB with its booster as second stage and the Mini-FTB alone as third stage;
- Mini-FTB shape: the Mini-FTB and the FTB_2 (i.e. the configuration of CIRA USV for the SRT mission) has to be drawn to 1:5 scale;
- propulsion system: the Mini-FTB has to be equipped with an external propulsion system to be activated after the Mini-FTB has been released from the carrier. The propulsion system has to be able to provide the Mini-FTB with the total impulse necessary to reach the required sub-orbital conditions;
- reaction control system (RCS): the Mini-FTB has to perform autonomous attitude control by means of a reaction control system, which has to be used both for the boosted and the ballistic phase. The RCS ought to be a cold gas system;

- aerodynamic flight control surfaces: the Mini-FTB has to perform autonomous flight and attitude control by means of aerodynamic control surfaces when it is possible;
- thermal protection system (TPS): the Mini-FTB has to be equipped with a TPS, if it is necessary;
- parachute load: the maximum force at parachute's deployment has to be lower than 75 kN;
- project cost: Mini-FTB has to be a low cost system. Thus it must use COTS equipments and state of the art technologies;
- wing loading similitude: in order to meet the wing loading similitude between Mini-FTB and FTB_2, Mini-FTB has to weight about 50 kilograms during re-entry;
- inertial loads similitude: in order to meet the inertial loads similitude between Mini-FTB and FTB_2 during re-entry, the values of the Mini-FTB principal moments of inertia has to be as follows: J_1 (pitch)=10 ± 20% kg·m², J_2 (yaw)=10.4 ± 20% kg·m², J_3 (roll)=0.8 ± 20% kg·m².

III. Mission Profile and Simulation

A. Mission Profile

The proposed mission profile is here illustrated:

- pre-flight operations;
- launch of the whole system, constituted by the stratospheric balloon, the nacelle, the Mini-FBT and its engine, from Trapani-Milo base;
- heating of the Mini-FTB and its engine during the ascent phase;

Figure. 2: Mini-FTB (STAR17)

Figure 3: Mini-FTB/A (STAR17A)

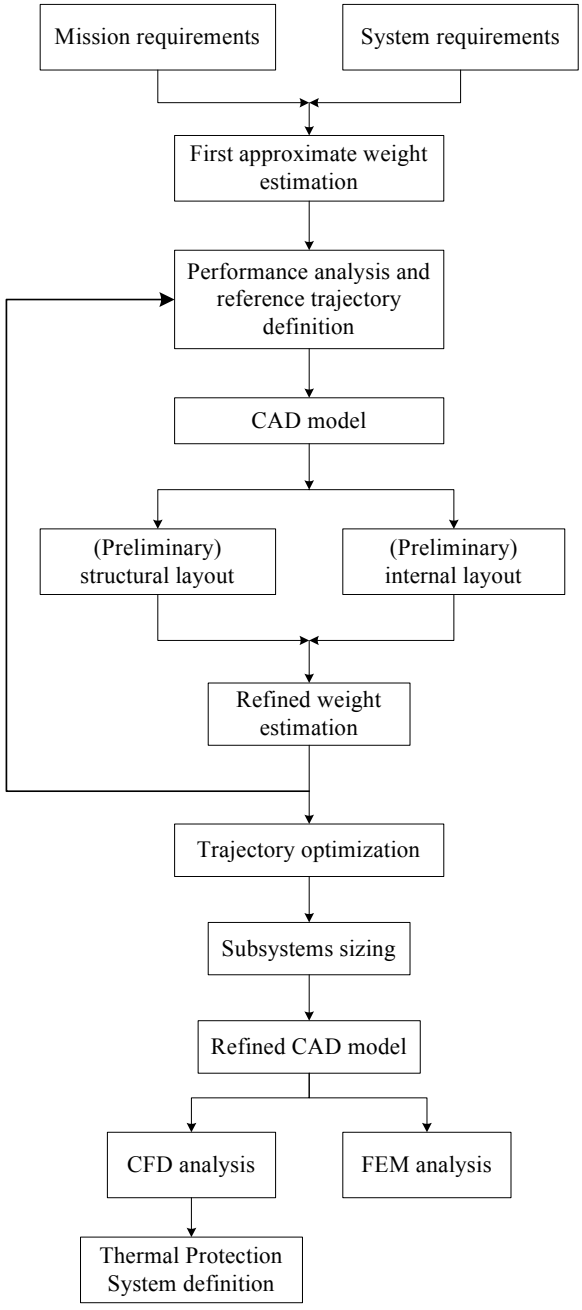

Figure 1: design process flow chart

- on-board systems' bootstrap and booting of the inertial platform just before the Mini-FTB is released from the carrier;
- heading control by means of the RCS system;
- at the nominal release altitude, checking of the correct trim and starting of the countdown;
- mechanical separation between the nacelle and the second stage;
- free dropping of the second stage for one second;
- engine ignition (11 kN thrust for 18 second). The RCS system makes the demonstrator follow the nominal climb trajectory, allowing the demonstrator reach sub-orbital condition (about 120 Km altitude in accordance with the sub-orbital ceiling height requirement);
- engine cut off and separation between the Mini-FTB and the engine itself;
- ballistic trajectory. The attitude control system operates in impulsive mode;
- re-entry phase, where maximum thermal loads are reached;
- parachute system's deployment at Mach < 0.6 and at 10000 m of height;
- Mini-FTB splashdown;
- Mini-FTB recovery.

B. Mission Simulation

In order to simulate the mission, the vehicle guidance problem must be solved. To this end, following common practice, open-loop guidance solutions have been preliminarily adopted to evaluate system performance. Thus, the main objective of the guidance study has been to identify the trajectories the demonstrator has to fly in order to meet the SRT mission objectives, provided that mission requirements and system constraints are not violated. As a consequence, mission objectives and requirements and reduced-scale system constraints have been integrated and translated into guidance solutions relying on optimization techniques[2]. The guidance study has been separately performed for the ascent and re-entry phases. Indeed, given the SRT mission profile, in these two phases different forces add to gravity in shaping the vehicle trajectory. In addition, different mission requirements and constraints must be considered. In particular, during the ascent phase the specific mechanical energy at the maximum altitude has been selected as the merit function, whereas the flight-time spent at thermal fluxes higher than a given threshold has bee selected as the merit function during the descending phase.

In order to improve demonstrator overall performance, the vehicle guidance has been performed using both AOA (angle of attack) and bank angle modulation to shape the trajectory. To this end, an AOA nominal profile, based on mission objectives and system constraints, is selected to be subsequently used as input to the optimization problem, whose solution returns the bank angle nominal profile[2]. The selected AOA and bank angle profiles are provided in Fig. 4.

The mission simulation results show that the proposed flight profile is feasible and compliant with the mission requirements, as Fig. 5 illustrates for the dynamic pressure requirement.

Figure 6 shows the comparison between the Mini-FTB, Mini-FTB/A and the FTB_2 trajectory.

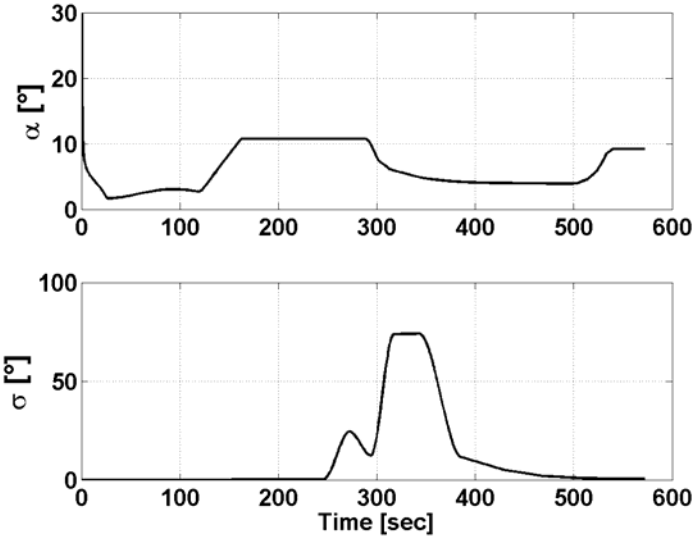

Figure 4. AOA and bank angle's profiles

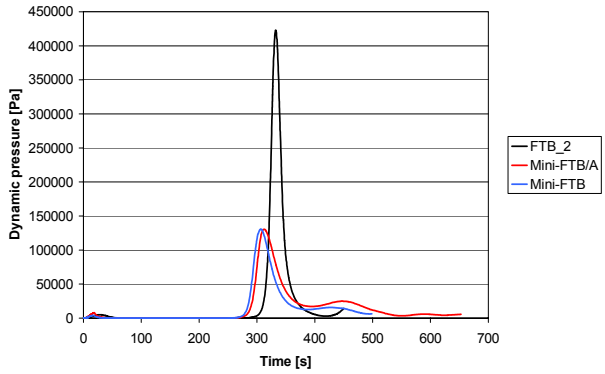

Figure 5: dynamic pressure's values comparison

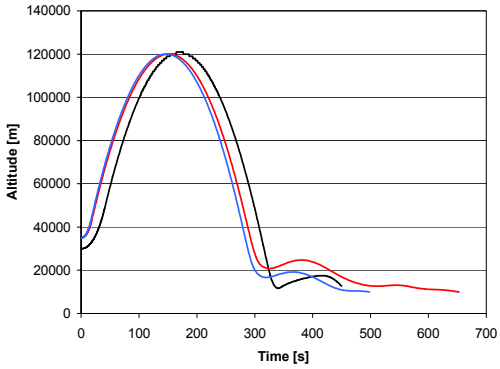

Figure 6: trajectory comparison

IV. Configuration

The external configuration of Mini-FTB and FTB_2 are the same. Except for some details, Mini-FTB and FTB_2 are drawn to 1:5 scale. The rear part of the Mini-FTB has been partially modified with respect to FTB_2 in order to allow the external propulsion system's installation. The nose is designed to be interchangeable. It is possible for the nose to maintain the same shape of the one of FTB_2 (1:5 scale) to test aerodynamic characteristics. Conversely, it is possible for the nose radius to be drawn to a different scale to test materials under severe conditions.

Mini-FTB main characteristics are:

scale:	1:5
length:	1.6 m
wing span:	0.71 m
reference wing area:	0.14 m^2
fuselage height:	0.19 m
fuselage width:	0.2 m
maximum height (empennages):	0.32 m
shape:	similar to FTB_2
basic material:	Incoloy® MA956 (TPS substrate)/AISI 316 steel (structure)
TPS:	TBC and/or Ceramic Matrix Composites (CMC)

Figure 7, Fig. 8 and Fig. 9 illustrate the Mini-FTB 3D CAD model[1].

Figure 7: side view of the Mini-FTB

Figure 8: side view of the Mini-FTB and its propulsion system

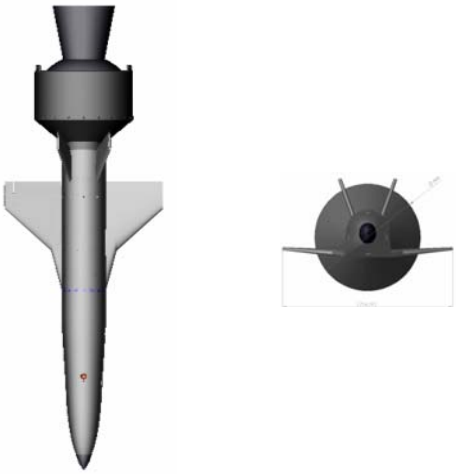

Figure 9: upper and front view of the Mini-FTB and its propulsion system

V. Structural Design

The driving factor of Mini-FTB structural design, in compliance with the philosophy of the project, is to keep cost as low as possible to satisfy design requirements. Commercial off the shelf materials have been widely used, as well as state of the art technologies.

Mini-FTB has been designed to be constituted by four main parts (see Fig. 10) to be assembled: forward body, wing/main body, rear body/empennages, power system. Figure 11 illustrates the Mini-FTB structural layout without systems and external skin.

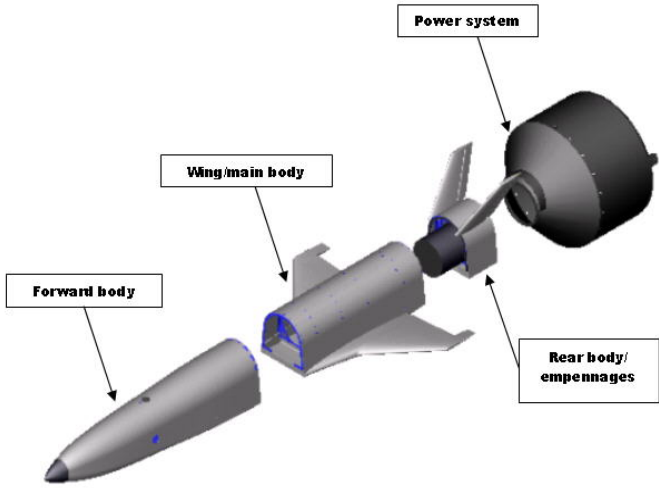

Figure 10: Mini-FTB four main parts

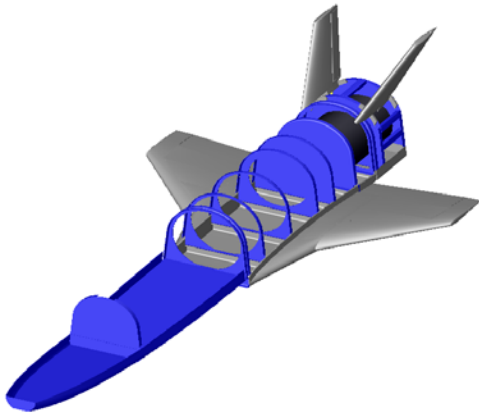

Figure 11: Mini-FTB internal structure

VI. Onboard Systems

Taking into account safety, the philosophy of the onboard systems design has been to keep it simple in order to reduce design and manufacturing's time and cost.

To perform the mission, the Mini-FTB needs the following onboard subsystems: Power System (PS), Electrical Power System (EPS), Reaction Control System (RCS), Flight Control System (FCS), Data Handling System (DHS); Tracking Telecommunication and Control System (TT&C), Guidance Navigation and Control System (GN&C), Recovery System (RS). For all of them, reference off-the-shelf components have been chosen in order to confirm the feasibility and the availability of the whole system. Figure 12 illustrates the Mini-FTB internal layout.

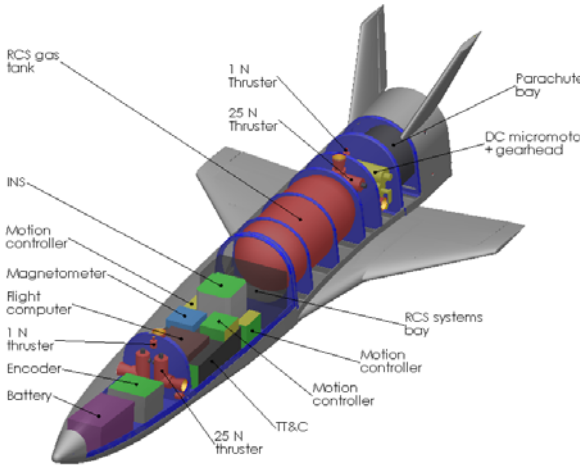

Figure 12: Mini-FTB internal layout

A. Power System

In order to perform the mission, Mini-FTB is equipped by an expendable rocket motor produced by ATK Thiokol Propulsion. As already mentioned, both the STAR17 and STAR17A apogee kick engine models have been chosen. Their main characteristics are shown in Table 1 and Table 2.

The STAR17 model is used for a less demanding mission. In order to improve performances the STAR17A model can be used (please note that, in this case, the demonstrator-engine attachment has to be modified).Unlike the power system of FTB_2, both STAR17 and STAR17A are not equipped by a TVC system. To overcome this drawback, the Reaction Control

Burn time:	17.6 s
Maximum thrust:	12348 N
Total impulse:	190.68 kNs
Weight (structure and propellant):	79.0 kg (84 kg with adapting structure)
Weight (propellant only):	69.6 kg
	

Table 1: STAR17 main characteristics

Systems has to be installed onboard the demonstrator and used during the boosted phase. Unlike the power system of FTB_2, which is placed inside the vehicle, the dimensions of the STAR17 and the STAR17A make it impossible to house the engine inside the demonstrator's body. Therefore an adapter is necessary (see Fig. 10).

Burn time:	19 s
Medium thrust:	16810 N
Total impulse:	319.38 kNs
Weight (structure and propellant):	126.1 kg (131 kg with adapting structure)
Weight (propellant only):	112.2 kg
	

Table 2: STAR17A main characteristics

B. Electrical Power System

The electrical power system is constituted by (Fig. 13): battery packages, one transformer and an electronic discharge control.

The Electrical Ground Support Equipments (EGSE) and the nacelle are used to provide electrical power respectively during pre-flight operations and during the ascent phase until the demonstrator is released from the balloon. Then, the onboard batteries become the main electrical power source for all flight. Onboard batteries supply 28 Volt (DC current). A transformer is thus necessary to supply 5 Volt for onboard electronics. A discharge electronic control device is useful to control and stabilize the current during battery discharge.

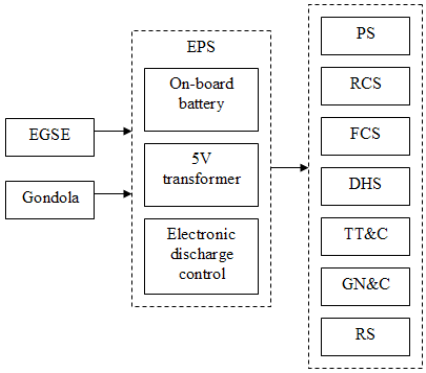

Figure 13: Electric power subsystem

C. Reaction Control System

Taking into account that the rocket engine does not have the TVC system, useful to maintain the nominal trajectory during the boosted phase notwithstanding the disturbance torques which arise from the not-aligned thrust, a reaction control system has been installed onboard the demonstrator. Another reason for the employment of the RCS is the impossibility of using the aerodynamic control surfaces of the vehicle to control it during the transatmospheric flight, i.e. where the air density is too low. Figure 14 illustrates the RCS system's architecture.

The propellant is stored in a titanium tank (S) at 6000 psi. The gas pressure is reduced to 1350 psi by a first pressure regulator (R1) to feed the block of thrusters T2 (25 N Thrusters), used for vehicle attitude control during the ascent boosted phase (continuous mode thrusting). A second pressure regulation, down to 300 psi, is performed by a second pressure regulator (R2) to feed the block of thrusters T1 (1 N thrusters), used for attitude control during the ballistic phases of the mission (pulsing mode thrusting). It should be remarked that the tank in the RCS schematic is spherical, but the tank selected to be integrated on board the vehicle is cylindrical (see Fig. 12) since this geometrical shape fits better inside the vehicle. Figure 15 shows the internal layout of the RCS thrusters: please note that the eight bigger thrusters (red in the figure) are the ones

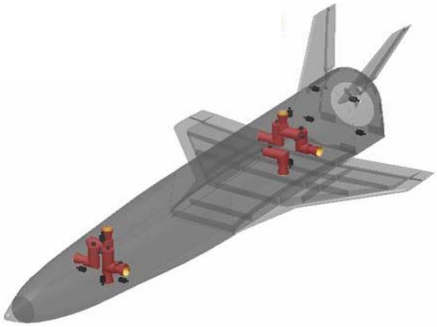

Figure 15: internal layout of the RCS thrusters

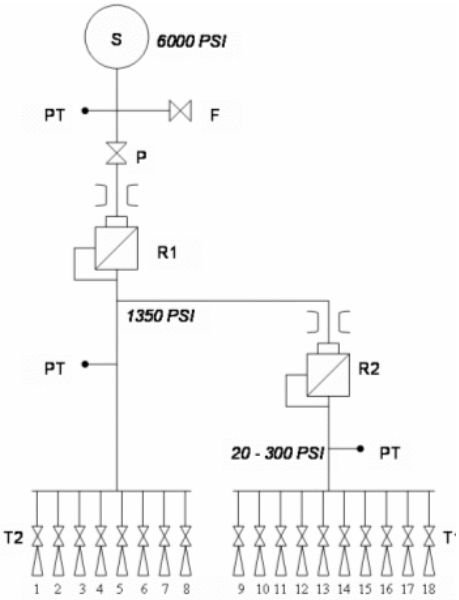

Figure 14: RCS architecture

dedicated to attitude control during the boosted phase, while the other ten thrusters (black in the figure) are the ones dedicated to the attitude control during the ballistic flight.

D. Flight Control System

During the atmospheric flight the demonstrator's attitude control is guaranteed by the aerodynamic surfaces: two elevons are dedicated to the roll control, if moved asymmetrically, and to the pitch control, if moved symmetrically, whereas the two aerodynamic surfaces of the butterfly tail allow the yaw control, if moved both to the same side, and the pitch control, if moved to opposite sides. All aerodynamic control surfaces are actuated by three DC electrical motors: one actuates both rudders and the others actuate the elevons, as shown in Fig. 16.

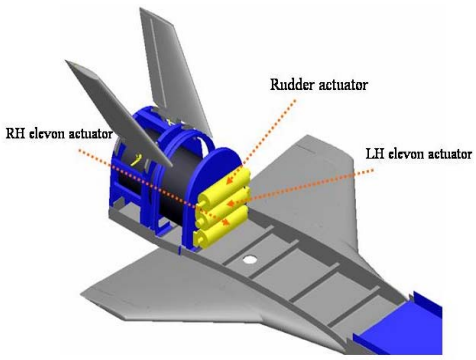

Figure 16: Flight control system's electrical actuators

E. Navigation System

GN&C components selection has been driven by technological simplicity and cost considerations. To this end Commercial-Off-The-Shelf (COTS) components have been selected as far as possible. Table 3 lists some relevant characteristics of the MiniSRT navigation system, which relies on a miniature, tactical grade INS (BEI Systron Donner™ DMI™), consisting of MEMS (Micro-Electro-Mechanical System) gyros and accelerometers, and on a miniature continuous-tracking GPS receiver (Trimble™).

	INS – Physical Characteristics and performance	
Size	81mmx90mmx98mm	
Mass	1 kg	
Power	17 W@ 28 VDC	
	Gyro	Accelerometer
Bias repeatability	10 deg/hr (1 sigma)	1.5 mg (1 sigma)
In-Run Stability	3 deg/h (1 sigma)	200 □g (1 sigma)
Scale Factor	350 ppm (1 sigma)	350 ppm (1 sigma)
Random Walk	0.035 deg/ $\sqrt{\text{hr}}$	60 □g/ $\sqrt{\text{hr}}$
Non-orthogonality	0.2 mrad (1 sigma)	0.2 mrad (1 sigma)
	GPS receiver features	
Size	25.4mmx25.4mmx6.9mm	
Mass	5.7 gr, including the shield	
Frequency	L1, C/A code, 12-channel, continuous tracking receiver	
Update rate	1 Hz (assuming enough processor time)	
Power	68 mW typical, 86 mW maximum @ 3.3 V	
Horizontal accuracy	Better than 7 meters CEP[a] 95%	
Vertical accuracy	Better than 10 meters CEP 95%	
Velocity accuracy	0.1 m/s	

[a]CEP = Circle of Equivalent Probability

Table 3: Navigation system main characteristics

Navigation system performance have been numerically investigated in order to verify if the selected hardware is adequate to provide accurate navigation during the whole mission. Three navigation modes have been considered: standalone GPS, standalone inertial and GPS-aided inertial navigation. Indeed, considering the short duration of the mission, comparison of performance of the last two navigation modes is of great interest. When the system operates in the first mode, accurate position and velocity fixes are output at 1 Hz data rate but no information about the vehicle attitude is available. Standalone inertial navigation returns full state measurements (position, velocity, and attitude) once it has been initialized, but it suffers from accuracy degradation with time[4]. The integrated configuration combines the advantages of both systems, even if an adequate measurement integration technique

must be selected and a considerable increase of the computational load must be accepted. Usually, navigation measures are integrated by means of Kalman filtering [5].

Navigation Mode		*GPS*	*Standalone inertial*		*GPS-aided inertial*	
Data rate		*1Hz*	*10 Hz*		*10 Hz*	
		RMS error	*RMS error*	*Max error*	*RMS error*	*Max error*
Horizontal position	m	7.5	$2.4\ 10^3$	$4.0\ 10^3$	$1.5\ 10^3$	$3.8\ 10^3$
Altitude	m	7.5	$4.0\ 10^3$	$7.3\ 10^3$	$8.2\ 10^2$	$1.7\ 10^3$
Attitude	°	n/a	$1.0\ 10^{-1}$	$5.2\ 10^{-1}$	$1.0\ 10^{-1}$	$5.2\ 10^{-1}$
Velocity	$\frac{m}{s}$	3.5	6.8	$2.2\ 10^1$	5.5	$1.5\ 10^1$

Table 4– Error statistics for each available navigation mode

Navigation performance has been estimated by means of Montecarlo analysis[6]. To this end, a series of navigation simulations have been carried out in order to estimate the resulting accuracy. Inertial sensor output has been computed using the INS Toolbox for Matlab™ by GPSoft™ [7]. For the adopted inertial unit random noise, bias, and scale factor errors have been modeled. The GPS receiver has been simulated by means of GPS Toolbox for Matlab™ by GPSoft™ [8]. Satellite positions have been computed using a real almanac. Ionospheric delay, tropospheric delay, receiver clock drift, and receiver efficiency have been modeled in the simulation of measured pseudoranges. Inertial navigation has been realized according to the model reported in Ref. 5, whereas the fusion algorithm has been written considering the models reported in Ref. 9 and Ref. 10. In particular, inertial sensor error dynamics has been modeled by means of the "phi" model[6].

Table 4 accounts for the error statistics of the three above described navigation modes. It is worth noting that GPS aiding mainly improves the accuracy of the standalone inertial navigation vertical channel. Indeed, the latter suffers from the well-documented accuracy instability with time[4]. Notwithstanding, a significant accuracy improvement can be observed also in the horizontal position and velocity estimates. Moreover, GPS aiding also improves the accuracy in the AOA determination, that is in the order of 0.1°. The impact of the GPS aiding on the attitude accuracy can be neglected, since the level of random-walk of the selected gyros allows for a measurement degradation in the order of 0.1° at the end of the mission.

F. Other Systems

1. Data Handling System and Tracking Telecommunication and Control System

The Data Handling System is composed by sensors and by one telemetry modular encoder, which sends data via to the TT&C system serial interface. The telemetry system works as a real-time transmission. The tracking is performed by the transmission of an IFF signal, in accordance with the IFF requirements and procedures. The demonstrator can also be controlled from a ground station to guarantee safe abort for emergency procedures.

2. Recovery System

The Mini-FTB is equipped with a recovery system, based on a double staged not guidable parachute. The entire parachute system has to be contained in a cylinder of three liters of volume, closed by a removable panel, with three attachments points. That cylinder is located in the rear part of the demonstrator, mounted axially to the fuselage (Fig. 17). The proposed solution allows:

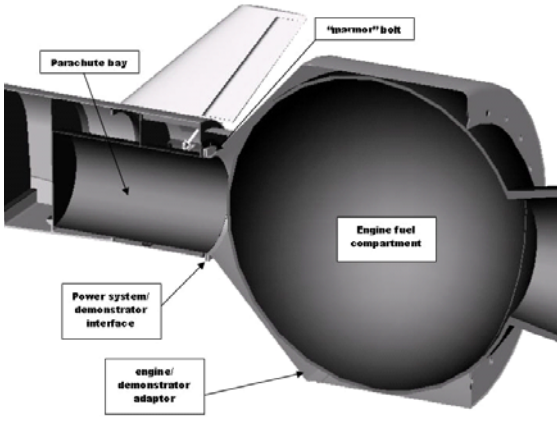

Figure 17: recovery and power system CAD model

- the power system to be easily and precisely installed and safely separated by means of a Marmor belt;
- the demonstrator to be airtight and watertight after the parachute has been extracted.

According to the mission requirements, the parachute must be opened at mach 0.6 and at a height of 10000 m. It must be a sequential opening: before a pilot chute and then a main chute. A rocket system has to be used for

extraction. In compliance with the systems requirements, the maximum force at deployment must be less than 75 kN.

VII. Interfaces

The Mini-FTB demonstrator and his booster must be carried by a balloon at altitude higher than 20 Km, where the lift of the balloon and the weight are in equilibrium (ceiling level).

In order to chose the type of balloon to be used, it is necessary to evaluate the balloon volume at ceiling level. The equilibrium condition is:

$$W = S = P_S = \omega = V\gamma_z(1 - \varepsilon) \tag{1}$$

where W is the weight of payload, P_s the Archimede lift, w the weight of the gas, V the volume of the balloon, γ_z the specific weight of the atmosphere at ceiling level and the ε ratio between the specific weight of the filling gas and those of the atmosphere at ceiling weight. As an example: $\varepsilon = 4.5:5$ for helium and for $\varepsilon = 8:9$ hydrogen; these value are a little lower than the pure gas values due to the osmosis effects across the cover.

The above equilibrium equation gives the value of the balloon volume and radius , assigning the level and the weight. Assuming for instance a total weight (engine + demonstrator + nacelle) of 200 Kg (conservative assumption) and a level of 30 Km, where the atmospheric density is $\rho = \gamma / 9.81 =$ 0,018 Kg/m^3, the radius R= 15 meter is obtained with the balloon filled with helium.

Balloons satisfying a similar requirement can be found on the market, such as the R = 19.6 m and consequently volume V = 31500 cubic meter Raven balloon. Moreover the IAP Xianhe Observatory stratospheric balloon can be taken into account. This is a 30,000 m^3 volume balloon which can reach up to 40 km of altitude and bring 220 kg of loads (it is used from 2000 for aeronomy studies at stratospheric level).

In order to dimension the suspension system the centre of the mass location and principal moment of inertia of the Mini-SRT must be measured by experimental tests. Namely the system must be balanced with precision to allow a good connection with the balloon; in particular, the centre of the mass of the assembly must be aligned with the suspension point. The trajectory optimization requires a specific pitch angle α_0 at the engine ignition, then the suspension system must comply with this requirement.

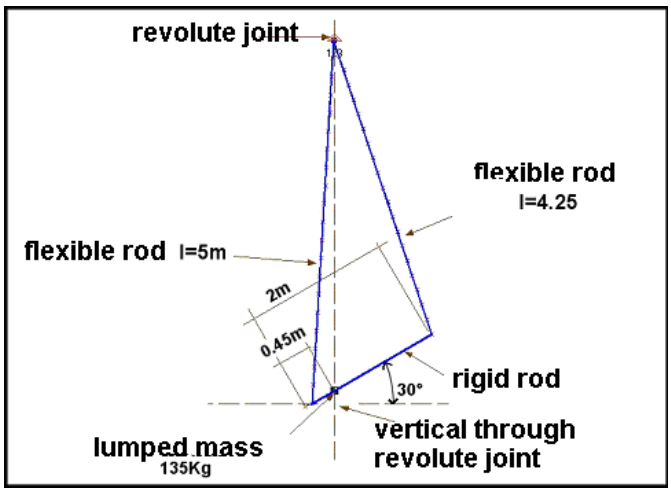

Figure 18: Rods structure

Following the National Scientific Balloon Facility (USA) regulations, the adoption of rigid suspension made by two aluminum 6061 T6 rods, is preferred. These rigid suspensions are located in order to have the demonstrator centre of the mass exactly below the suspension point and to have at the same time the demonstrator maintained with a α_0 angle from the horizontal line.

The L distance from the suspension point has been selected in order to have a trajectory tangent with the balloon, at release time. The balloon is considered as a sphere with R radius; considering , for instance, $\alpha = 42^o$ and R = 15 m, the length *L* results of 5 meters; thus one rod is long 5 meters, the second rod has length of about 4.25 meters, see Fig. 18.

The two rods are made by carbon with the following characteristics: density = 1650 Kg/m^3, Joung modulus = 1.8e+11. The section dimensions of two rods are: diameter *d* = 8 cm, thickness *t* = 5 mm. The weight of the main rod is 10.5 Kg, while the weight of the second rod is 9 Kg.

To take care of a high value of the load factor during the balloon ascent phase the aircraft weight multiplied by a factor 5 in the static analysis. Consequently the static analysis considers a vertical load of *F* = 137*5 Kg and

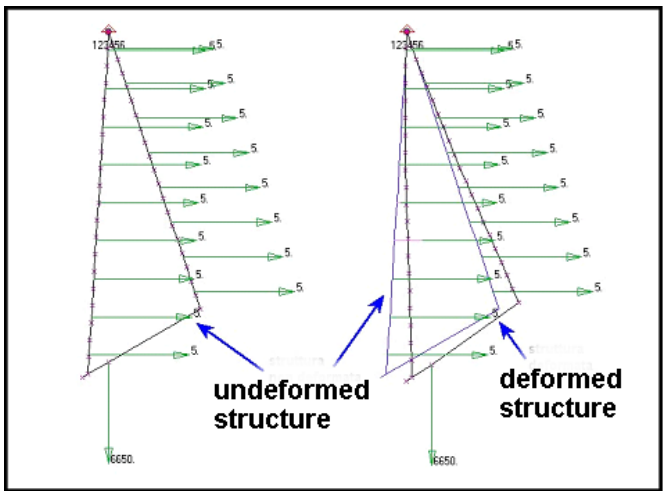

Figure 19: Rods deformation

considers aerodynamic loads as consequence of lateral wind of 80 m/s, according to JAA (Joint Aviation Authorities) specifications. The aerodynamic load D from lateral wind has been calculated in the following condition: Level: 15.000m , Speed: 80 m/s, Cd: 3.5 , Atmospheric density: $1x10^{-1}$ Kg/m^3, Area: 0.4m^2.

The result is a load of near 5 N, distributed in both rods; according to this hypothesis, the deformation of the structure appears as shown in Fig. 19. Characteristic structure values are: maximum deformation: 1.93 mm, maximum stress: 7.3 Mpa. It is evident that the maximum stress is below the ultimate stress of the material.

The dynamic analysis has been performed applying on the rod a 200 Kg load. The following results showed the natural frequencies of the vibration of the structure:

Mode 1=19.7336 Hz, Mode 2 = 20.9312 Hz, Mode 3 = 33.1131 Hz, Mode 4 = 55.3522 Hz, Mode 5= 76.0250 Hz, Mode 6= 78.607 Hz, Mode 7 = 84.20602 Hz.

The length of two rods and the demonstrator trim do not assure a trajectory without interference with the balloon because, after the release, the balloon for elastic effect will deform its shape especially in the horizontal plane.

Nevertheless, it is preferred to foresee, after the release, a free drop for a short time of the demonstrator, rather than extend the vertical rods length. This solution is chosen also in order to limit the lateral loads. Spherical joints are foreseen with the purpose to reduce these loads and the turbulence effect of the balloon on aircraft-propeller system. The balloon during the ascent maneuver suffers the action of the winds at high level that, in addition to the translation movement, transmit to the balloon a rotation, generally around the suspension axis if the system is well balanced. This rotation at maximum is of 2 revolution per minute; the spherical joints permit to decouple the rotational movement of the balloon from those of the demonstrator; for this reason it is possible to foresee a rotation speed less than 2 rpm.

At the release time, that rotation speed must be zero and the point angle must be the requested one. The trim control system in this phase must operate using a 1 N thrusters located on the top of the SRT.

At the release time, the system is in equilibrium, with a transverse speed of about 10 m/s. The assembly rotates through the gravitational axis with the certain angular speed $\dot{\psi}_o < 2rpm$ and in absence of couples:

$$I\ddot{\psi} = 0 \tag{2}$$

In the development of the mission analysis a specified pointing angle ψ is required. After the acquisition of this angle with the zero angular speed, the demonstrator-propeller is ready to be released from the balloon. The controlled system will be then:

$$I\ddot{\psi} = u \tag{3}$$

Where u is the couple made by the thrusters located in the front position. The proposed control logic is based on optimum control of low response time bang-bang type; this approach requires to switch on the trim thrusters at maximum thrust in the direction opposite to the movement until the defined trim is reached; then the use of opposite thruster will permit the pointing acquisition with the rotation speed near to zero. The point of the thrust direction reverse (switch point) is highlighted on phase plane $(\psi, \dot{\psi})$ as intersection point between the parabola obtained by integration of the system

$$\dot{\psi} = r$$
$$\dot{r} = (T * b) / I \tag{4}$$

and the switching function:

$$\dot{\psi}^2 = 2(T * b / I) * \psi \tag{5}$$

In this case, the thrust is equal to T = 1 N, the harm b = 1.15 m and the moment of inertia related to the vertical axe of the aircraft-propeller-rod is: $I = 30Kgm^2$.

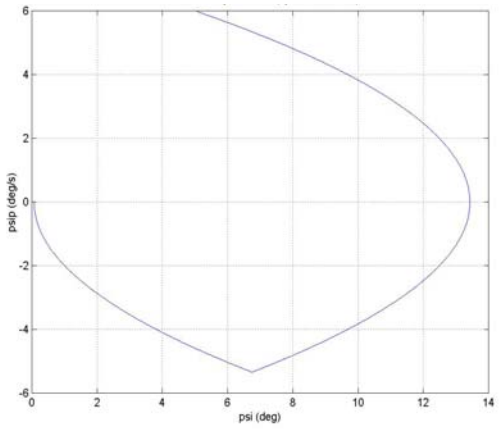

Figure 20: Phase Space and Switching Point

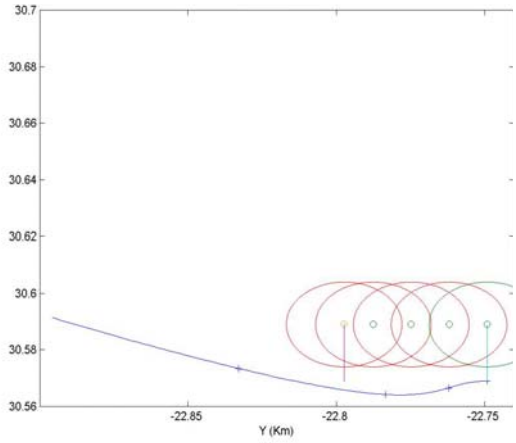

Figure 21 : The system trajectory after the balloon separation

Considering the initial conditions of rotation $\dot{\psi}_o = 6\,\mathrm{deg}/s, \psi_o = 5^o$ and the requested pointing angle ψ_i=0° (launch in north direction), the Fig. 20 is obtained.

The figure shows that the demonstrator pushed by the right engine rotates anticlockwise until the maximum angle of 14° is reached; later the angle will be reduced to 6°. Therefore, pushing by the left engine, the desired angle will be obtained with the accuracy of 0.05°, and 0.01° degree per second of residual speed. It is possible to obtain a limit cycle that meets the desired condition with the best precision after the repetition of the process. In Fig. 21 the pointing maneuver requests 7.8 seconds. It is important to note that, at release time, the demonstrator flight angle γ is near zero because the speed vector is in the horizontal plane and the angle of attach α is 42°, angle of transportation of the demonstrator. The balloon horizontal speed vector is not generally in the plane of requested trajectory defined by a pointing angle ψ_i, but with a component out of the plane with a trajectory different form desired one

Nevertheless, being the balloon residual speed of modest entity compared with the speed reached during the propulsion, the demonstrator trajectory plane at the end of the propulsion phase will be near the requested trajectory. Nevertheless, being the balloon residual speed of modest entity compared with the speed reached during the propulsion, the demonstrator trajectory plane at the end of the propulsion phase will be near the requested one. This is confirmed by numerical simulations carried out that show an error between the final trajectory plane and the desired one of one degree maximum. The conclusion of this investigation is that it is not necessary to search a pointing angle different than ψ_i, in order to obtain the desired value at the end of the propulsion phase.

After the requested pointing acquisition, the assembly demonstrator-booster can be released from the balloon. The assembly demonstrator is fixed to the rods through two rings closed in the lower part by explosive bolts. After the explosion of the bolts, the belts will be opened by the weight force and, if necessary with adding special springs, the demonstrator will be free.

In order to avoid a balloon impact and at same time to have the possibility to balance disturbance caused by the release, a free drop of 0.5 seconds is scheduled. During this time the demonstrator drops approximately 5 meters; the separation of L = 10 meters from the release point will assure a transit at the distance d = 43 m from the centre of the balloon.

A numerical simulation of the release trajectory has been made; in this simulation an extension in x-y direction of 30% of the balloon radius and a balloon speed parallel to the thrust direction (in other words with the same azimuth angle ψ_i) have been considered.

The results of the simulation are shown in Fig. 21; the balloon centre of the mass locations versus time (labeled with symbol "0") have to be compared to the demonstrator centre of the mass at the same time (labeled with symbol "+"). The result is a safe trajectory. In the simulation it has been supposed that angles and angular speed of the demonstrator out of the plan of symmetry are zero and the demonstrator itself have no control of trim in the vertical plane. This last hypothesis is considered acceptable because the effect of aerodynamic load and moment are neglected in this phase as consequence of atmospheric low density at the considered level. The hypothesis of zero angles and zero angular speeds out of the symmetry plane is also acceptable considering that a control on the tree axes during the vertical drop phase is foreseen.

Considering the low disturbance (then linear equations) and neglecting the aerodynamic moments, tree copies of the previous control problem are to be considered, one for each axis:

$$I_x \ddot{\phi} = u_x, I_y \ddot{\theta} = u_y, I_x \ddot{\psi} = u_z, \tag{6}$$

It may be necessary to use thruster at 45 N, in the case of initial disturbance that doesn't allow the desired trim acquisition during the foreseen time or free drop. Surely the trim thrust will be used for the control of disturbance moment as consequence of thrust misalignment.

At the end of the propelled trajectory, in according to the guidance law, the assembly aircraft-booster will be at level of about 43 Km. At this point, it is foreseen the separation between the aircraft and the booster, in order to start with the gliding phase.

The attachment of the engine to the demonstrator is made by two parts; a cylindrical component fixed to the attachment ring of the engine and another conical component directly joined on the demonstrator by an elastic belt system .

The separation system is composed by one elastic belt and explosive bolts, V formed attachments, lateral and longitudinal springs. The elastic belt, made by steel and composed by two parts, is connected with explosive bolts.

The duty of the elastic belt consists joining the two parts, demonstrator interface and connection with engine components, pressing a V shaped attachment that prevents from the relative motion between the parts.

After the bolts explosion , the elastic belt releases the demonstrator. The separation is made easier by a separator spring. The two parts of the elastic belt are fixed to the structure by longitudinal springs to avoid collision with the demonstrator).

The system trim at the release time must be controlled in order to have zero nominal angular speed; in particular, the pitch angular speed must be near zero. The sizing of the separator spring can be made according to the consideration that at the end of its deformation the spring with the elastic module K end length l, will generate a speed change ΔV_1 on the engine (having at the fuel exhausted a mass equal to m_1.=15.7 Kg). and a speed variation ΔV_2 of the demonstrator (having a mass equal to m_2.=52 Kg) with opposite sign :

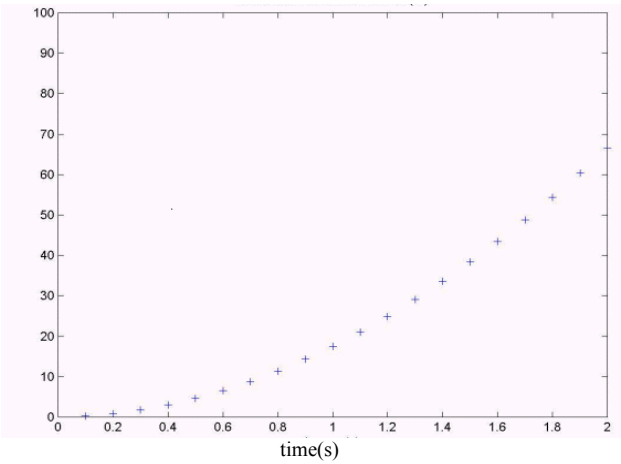

Figure 22: Mini SRT-engine distance (meters) after two second

$$\Delta V_1 = -l\sqrt{k}\sqrt{\frac{m_2}{m_1}\frac{1}{m_1+m_2}} \tag{7}$$

$$\Delta V_2 = l\sqrt{k}\sqrt{\frac{m_1}{m_2}\frac{1}{m_1+m_2}} \tag{8}$$

For example, considering a WP-Andreani type spring with length l=0.1m and K=650 N/m , the following values are obtained: ΔV_1=-0.56 m/s e ΔV_2=-0.17 m/s.

These variation speed, associated with the bigger aerodynamic drag of the released engine compared to the aircraft drag, assure the trajectory separation of two bodies.

In the Fig. 22 the growth with time (from separation) till two seconds of the distance between the demonstrator and the engine is shown.

VIII. Weight Estimation

Table 5 shows the weights breakdown for Mini-FTB, considering both options (Nitrogen and Freon 14) for the cold gas of the RCS System, while Table 6 shows the weights breakdown for Mini-FTB/A, considering only the Freon 14 cold gas for the RCS System.

Structure (no optimisation):	27 kg
RCS (Nitrogen):	10.6 kg, 7.4 kg (dry)
RCS (Freon 14):	18 kg, 8.9 kg (dry)
Other systems:	12.2 kg
Payload:	2 kg
Mini-FTB (Nitrogen):	51.8 kg, 48.6 kg (dry)
Mini-FTB (Freon 14):	59.2 kg, 50.1 kg (dry)
Mini-FTB + power system (Nitrogen)	136 kg
Mini-FTB + power system (Freon 14)	143 kg

Table 5: Mini-FTB weights breakdown

Structure (no optimisation):	27 kg
RCS (Freon 14):	17.1 kg, 8.5 kg (dry)
Other systems:	12.2 kg
Payload:	2 kg
Mini-FTB (Freon 14):	58.3 kg, 49.7 (dry)
Mini-FTB + power system (Freon 14)	189 kg

Table. 6: Mini-FTB/A weights breakdown

IX. Aerothermodynamics

Aim of the paragraph is the presentation of the aerothermodynamic analysis results, in particular the investigation of the heat flux at stagnation point at nose and at wing leading edge. For this purpose analytical and computational methods have been employed. In particular the Fay-Riddel formula[11] and Fluent® software have been used. Conductive heat transfer is assumed to be negligible. Thus, the two main heat transfer mechanisms occurring onboard the vehicle are radiation and convection. Assuming convective heating to be the major source of energy input, the entry vehicle surface will continue to heat until the point where energy dissipation due to thermal radiation exactly balances the convective input.

A. Analytical Analysis Results

Applying the Fay-Riddel formula to the reference trajectory, the graph of the heat flux density at stagnation point at nose versus time and the graph of the altitude versus time were obtained (Fig. 23). The same parameters were calculated for the wing leading edge. The most critical condition is highlighted in Fig. 23: it obviously corresponds to the highest heat flux of about 350 kW/m^2. Figure 24 illustrates the variation of the heat flux density versus time for two different configurations of Mini-FTB: the thicker line corresponds to the case of the nose radius drawn to 1:5 scale (same case of Fig. 24), while the thinner line corresponds to the case of the nose radius drawn to 1:1 scale. As can be noted the latter case presents more severe conditions than the former, but it meets mission requirements.

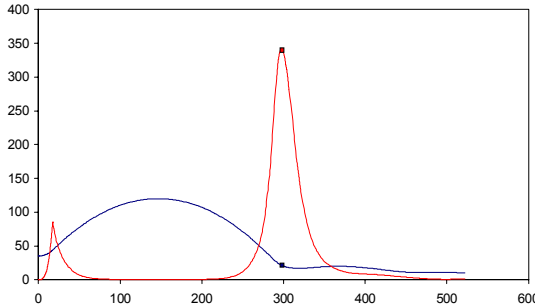

Figure 23: Variation of altitude (km) with time (seconds) (blue line) and variation of heat flux density at nose (kW/m^2) with time (seconds) (red line)

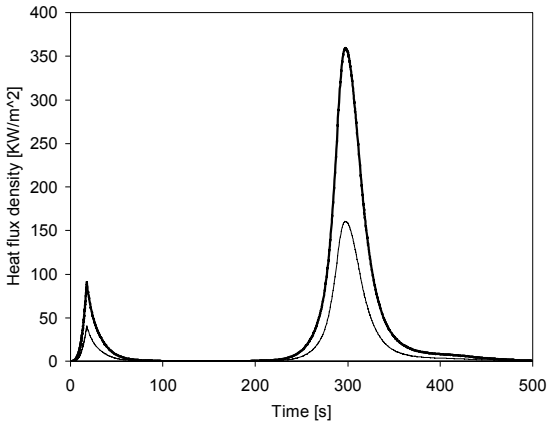

Figure 24: heat flux density versus time for the Mini-FTB (nose radius drawn to 1:5 and 1:1 scale)

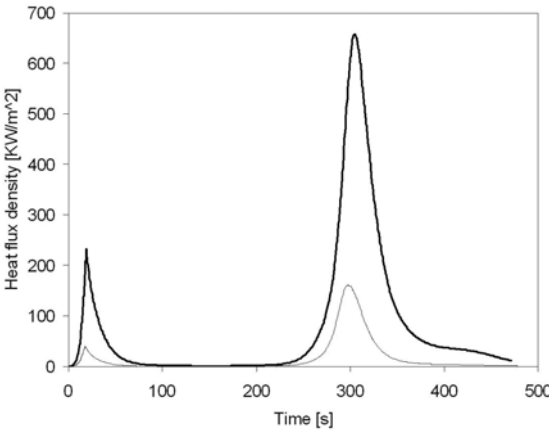

Fig. 25: heat flux density versus time for the Mini-FTB/A (nose radius drawn to 1:5 and 1:1 scale)

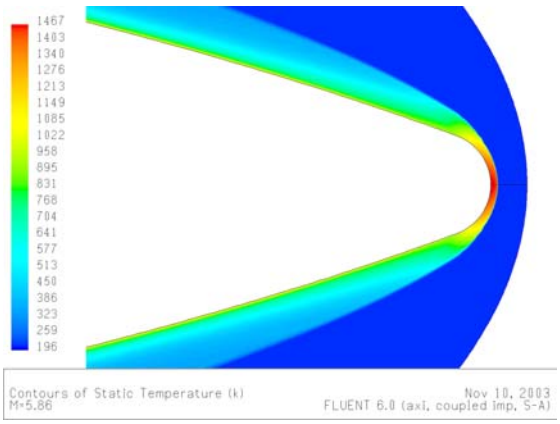

Figure 27: variation of the surface temperature along the body longitudinal axis for the demonstrator's nose (drawn to 1:1 scale) and front part

Figure 25 shows the variation of the heat flux density versus time for the Mini-FTB/A: the two configurations considered are the same as the ones in Fig. 24. The critical conditions have been investigated by extensive aerothermodynamics analyses carried out by the use of CFD programs (FLUENT®), under the supervision of a research group at DENER, Politecnico di Torino.

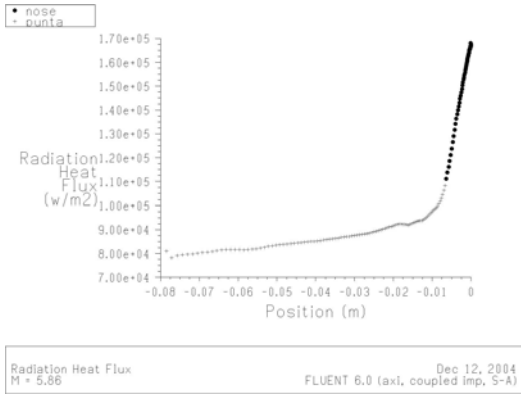

Figure 26: variation of the heat flux along the body longitudinal axis for the demonstrator's nose (drawn to 1:1 scale) and front part

B. CFD Analysis Results

For easy of work and calculus, the demonstrator's nose has been considered as an axis-symmetric body, thus implying that the angles of incidence of the external flux have to be assumed equal to zero. Angles of incidence of the external flux different from zero imply an apparent radius of curvature at stagnation point bigger than the real one. Although considering angles of incidence of the external flux equal to zero simplifies the problem, it does also help validate the analytical analysis. Fig. 26 illustrates the variation of the heat flux along the body longitudinal axis for the demonstrator's nose and front part. As can be noticed, the heat flux at the stagnation point is 168 kW/m^2. Comparing this value to the

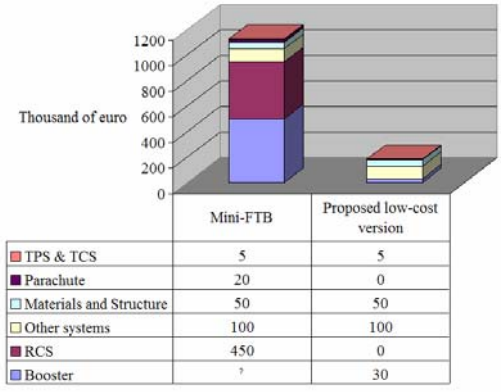

	Mini-FTB	Proposed low-cost version
TPS & TCS	5	5
Parachute	20	0
Materials and Structure	50	50
Other systems	100	100
RCS	450	0
Booster	?	30

Figure 28: first approximate cost estimation: Mini-FTB compared to a low-cost version of the demonstrator

result of the analytical analysis, 172 kW/m^2 (see Fig. 25, thinner line), it is possible to note that the difference is small, thus validating the analytical analysis. Figure 27 illustrates the variation of the surface temperature along the body longitudinal axis for the demonstrator's nose and front part.

X. Cost Estimation and conclusions

Leaving the cost of the booster out, it is possible to assert that the total cost of the demonstrator is mainly due to the RCS system (see Fig. 28).

To conclude it can be said that the present study has demonstrated the feasibility of Mini-FTB, as conceived to perform Mini-SRT mission. Its manufacture and test could surely be a decisive factor for the FTB_2 and SRT mission's success.

References

[1]Politecnico di Torino, Università di Napoli Federico II, Università di Roma La sapienza, "Mini-SRT feasibility study-Technical final report", April 2004.

[2]Tancredi, U., Accardo, D., Grassi, M., Curreri, F., "Longitudinal Dynamics and Navigation Performance Analysis for an Unmanned Space Vehicle", *Conference on Dynamics and Control of Systems and Structures in Space 2004*, 18–22 July 2004 Riomaggiore, Cinque Terre, Liguria, Italy.

[3]Remiti, F., "Studio di fattibilità di un dimostratore tecnologico sub-orbitale di dimensioni ridotte", *Final project in Aerospace Engineering*, Politecnico di Torino, July 2003.

[4]Merhav, S., "Aerospace Sensor Systems and Applications", *Springer Verlag*, New York, 1996.

[5]Savage, P.G. , "Strapdown Analytics", *Strapdown Associates Inc*., Maple Plain (MN), 2000.

[6]Chatfield, A.B., "Fundamentals of High Accuracy Inertial Navigation", *AIAA Press*, Washington DC, 2000.

[7]"Inertial Navigation System Toolbox for Matlab®", GPSoft, Inc, URL: http://www.gpsoftnav.com/inertial.html [cited June 11th 2004].

[8]"Satellite Navigation System Toolbox for Matlab®", GPSoft, Inc, URL: http://www.gpsoftnav.com/inertial.html [cited June 11th 2004].

[9]Farrell, J., Barth, M., *The Global Positioning System and Inertial Navigation*, McGraw Hill, New York, 1999.

[10]Rogers, R. M., "Applied Mathematics in Integrated Navigation Instruments", *AIAA Press*, Washington DC, 2000.

[11]Hankey W.L., *Re-entry Aerodynamics*, AIAA education series.